batteries

MDPI

Article

One-Step Synthesis of Zirconium Sulfide Nanoparticles on Flexible Carbon Cloth for Supercapacitor Application

Yu-Xuan Wang [1], Dung-Sheng Tsai [2], Chu-Jung Huang [1], Zi-Yu Chen [1] and Chuan-Pei Lee [1,*]

[1] Department of Applied Physics and Chemistry, University of Taipei, Taipei 10048, Taiwan; u11003001@go.utaipei.edu.tw (Y.-X.W.)
[2] Department of Electronic Engineering, Chung Yuan Christian University, Taoyuan 320314, Taiwan; dungsheng@cycu.edu.tw
* Correspondence: cplee@utaipei.edu.tw; Tel.: +886-2-2311-3040 (ext. 3912); Fax: +886-2-2389-7641

Abstract: Zirconium sulfide nanoparticles (Zr_xS_y) are prepared on a flexible substrate of carbon cloth (CC) via a one-step synthesis approach using the low-pressure chemical vapor deposition (LPCVD) technique. The scanning electron microscopy (SEM) image reveals that the particle sizes are in the range of ca. 3~23 nm with an average value of ~13.02 nm. The synthesized Zr_xS_y nanoparticles are composed of ZrS_3 and Zr_9S_2 phases, which is verified by X-ray diffraction (XRD) and high-resolution transmission electron microscopy (HR-TEM). By using the Zr_xS_y/CC as a supercapacitor flexible electrode, the capacitance extracted from the cyclic voltammetry measurement is 406 C g^{-1} at a scan rate of 5 mV s^{-1}; the capacitance values obtained from GCD curves at a current density of 0.5 A g^{-1} and 1 A g^{-1} are 151 and 134 C g^{-1}, respectively. These results highlight the promising potential of Zr_xS_y as a supercapacitor material for future energy-storage technology.

Keywords: low-pressure chemical vapor deposition; one-step synthesis; supercapacitor; zirconium sulfide

Academic Editors: Cornelia Bandas and Michele Vittadello

Received: 13 December 2024
Revised: 25 March 2025
Accepted: 30 March 2025
Published: 31 March 2025

Citation: Wang, Y.-X.; Tsai, D.-S.; Huang, C.-J.; Chen, Z.-Y.; Lee, C.-P. One-Step Synthesis of Zirconium Sulfide Nanoparticles on Flexible Carbon Cloth for Supercapacitor Application. *Batteries* **2025**, *11*, 138. https://doi.org/10.3390/batteries11040138

1. Introduction

In recent years, with the increasing global emphasis on low carbon technologies and green energy, the inherent limitations of traditional energy storage systems, such as batteries, have become increasingly evident in terms of charge–discharge efficiency, power density, and energy density. In contrast, supercapacitors, with their unique combination of double-layer capacitance and pseudocapacitive effects, show great potential for various applications. This has attracted considerable attention, especially with the rising demand for fast-charging energy storage systems in fields such as medical equipment, electric vehicles, and electronic devices [1–7]. The advantages of supercapacitors include improving cycle life and enhancing power for major power systems such as fuel cells and batteries. Electrochemical supercapacitors can be classified into two types based on their energy storage mechanisms [8,9], i.e., electric double-layer capacitors (EDLC) and pseudo-capacitors (PC). For an EDLC, when a voltage is applied to the electrodes, positive and negative ions in the electrolyte move toward different sides, forming a tightly packed charge layer that produces the capacitive effect. Since this process involves only physical charge transfer, there is minimal change in the volume or shape of the electrode material, resulting in a longer cycle life for EDLCs. As for a PC [10–12], this is a capacitor-like device in which a reversible and fast Faradaic reaction occurs on or near the surface of electrode materials when voltage is applied, producing the capacitive effect. Because a Faradaic reaction can occur both within the electrodes and on the surface, a pseudo-capacitor typically exhibits

higher energy density and specific capacitance as compared to an EDLC. More precisely, pseudo-capacitance is a Faradaic charge storage mechanism based on fast and highly reversible surface or near-surface redox reactions, and can be divided into the following three categories according to their charge storage mechanisms [8,13–16]: (i) underpotential deposition; (ii) surface redox pseudo-capacitance; and (iii) intercalation pseudo-capacitance. Surface redox pseudo-capacitance refers to the process of storing charge on the surface of the electrode material through continuous and reversible redox reactions.

Recently, the promising electrode materials used for supercapacitors [17] are: (i) carbon-based materials; (ii) conductive polymers; (iii) transition metal oxides; and (iv) transition metal dichalcogenides (TMDs) [18–22], among others. TMDs have recently been used as the electrode materials for battery-like supercapacitors or pseudo-capacitors due to their excellent properties, such as a large surface area that ensures ample active sites for efficient charge transfer kinetics and electrochemical reactions, as well as exemplary chemical stability in electrochemical environments, which guarantees prolonged cycling stability and device performance [23,24]. Transition metal sulfides [15,25–30], such as MoS2 [31–34], SnS_2 [1,2,4,35], FeS_2 [36–38], Co_3S_4 [39–41], and Ni_3S_4 [42–44], are commonly used as electrode materials because of their high redox activity, high specific capacity, good electrical conductivity, unique crystal structures, and low electronegativity [15,45,46]. Metal sulfides offer superior electrochemical properties over metal oxides due to the substitution of oxygen with sulfur [18]. Key advantages include higher electrical conductivity, as sulfur forms weaker bonds with metals, allowing for greater electron delocalization [47]. Metal sulfides also have larger specific surface areas, providing more active sites for reactions and improving capacitance. Additionally, their unique electronic structure reduces charge transfer resistance, leading to better rate capability and power density, making them potential candidates for high-performance supercapacitor electrodes [48]. Additionally, TMDs possess higher electrical conductivity, enhanced thermal and mechanical durability, and more diverse redox chemistry compared to the corresponding metal oxides and carbon-based nanomaterials, making them ideal electrode materials for supercapacitors [49].

When selecting electrode materials, several factors such as cost, toxicity, and abundance in the earth's crust must also be considered. Up to date, research on zirconium sulfide-based supercapacitor electrodes is limited. To the best of our knowledge, only one study focused on ZrS_2-based electrodes for supercapacitor application. M. Habib et al. [50] successfully synthesized single crystal ZrS_2 nanoflakes using the chemical vapor transport method and investigated their performance as the electrode of a supercapacitor. Electrochemical tests revealed that the ZrS_2 electrode showed a remarkable specific capacitance of 18.8 C g^{-1} at 10 mV s^{-1}. In this work, zirconium sulfide nanoparticles (Zr_xS_y) composed of ZrS_3 and Zr_9S_2 phases are prepared on the flexible substrate of carbon cloth (CC) via a one-step synthesis approach using the low-pressure chemical vapor deposition method. By using Zr_xS_y/CC as a supercapacitor flexible electrode, the capacitance extracted from the cyclic voltammetry measurement shows 406 C g^{-1} at a scan rate of 5 mV s^{-1}. As compared to the previous report, the Zr_xS_y-based electrode composed of ZrS_3 and Zr_9S_2 phases exhibits much higher capacitance than that of the electrode with single crystal ZrS_2 nanoflakes. These results highlight the promising potential of Zr_xS_y as a supercapacitor material for energy-storage technology.

2. Materials and Methods

2.1. Materials

Sulfur powder (99.5% purity) and zirconium tetrachloride ($ZrCl_4$, 98.0%) were obtained from Alfa Aesar and Acros organics, respectively. Flexible carbon cloth substrate (CC, W0S1009) was obtained from CeTech Co., Ltd., Taichung, Taiwan. Argon

(Ar, 99.9995%) and hydrogen (H_2, 99.9995%) gases were purchased from Shenyi Gas Co. Ltd., Taipei, Taiwan.

2.2. Synthesis of Zirconium Sulfide (Zr_xS_y) Nanoparticles

An LPCVD system, equipped with a tube furnace and a quartz tube, is used to prepare the Zr_xS_y/CC electrode (Figure 1). The sulfur (S) and zirconium (Zr) precursors were sulfur powder and zirconium tetrachloride, respectively. During the growth process, sulfur was placed in an upstream alumina boat (i.e., Zone I) at a temperature of approximately 220 °C. A tungsten boat containing the Zr precursor was positioned at the center of the heating furnace (i.e., Zone II), and the vertically standing carbon cloth (CC) substrate was placed at the edge of the heating furnace (i.e., Zone III). The temperature program of Zone II was designed to increase from room temperature (RT) to 950 °C, hold at 950 °C for 30 min, and then cool down to RT. The process was conducted under a pressure of 30 torr with the gas flow of Ar (150 sccm) and H_2 (5 sccm). When Zone II reached 700 °C, Zone I was heated to 220 °C (5.5 °C min^{-1}) to facilitate the vaporization of the sulfur powder.

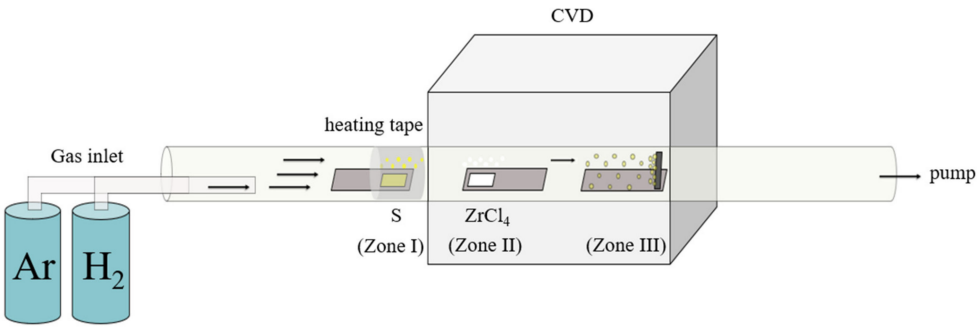

Figure 1. Chemical vapor deposition (CVD) system.

2.3. Material Characterization

To investigate the basic material properties, the composition and structure of the synthetic materials will be verified by high resolution transmission electron microscopy (HR-TEM, JEOL JEM-2100F, Taipei, Taiwan), field emission scanning electron microscope (FE-SEM, JEOL 7900F, Taipei, Taiwan), energy-dispersive X-ray spectroscopy (EDS, OXFORD X-MaxN TSR, Taipei, Taiwan), X-ray diffraction (XRD, D2 Phaser with XFlash, Bruker, Taipei, Taiwan), and Brunauer–Emmett–Teller (BET, NOVAtouch LX2, Quantachrome Instruments, Taipei, Taiwan).

2.4. Electrochemical Characterizations

Using a three-electrode cell system, all electrochemical measurements are performed by using an Autolab 204 potentiostat (Metrohm Autolab, Utrecht, The Netherlands). Without the use of any polymer binders or conductive fillers, a 3 × 1 cm^2 electrode with 1 × 1 cm^2 active area (Zr_xS_y loading mass: ~0.1 mg) was used directly as a working electrode. The surface area of Zr_xS_y/CC and pristine CC are 47.58 m^2 g^{-1} and 39.01 m^2 g^{-1}, respectively; these values are obtained via BET analysis. A Ag/AgCl electrode and platinum sheet are used as a reference electrode and counter electrode, respectively. The electrolyte is 0.5 M $H_2SO_{4(aq.)}$. Within the applied voltage range of −0.2 to 1.0 V, the cyclic voltammogram (CV) measurement was performed under various scan rates. The specific capacitance values are calculated by integrating the CV curve area using the following equation [51]:

$$Ca = \frac{1}{[2m\upsilon(V_a - V_b)]} \cdot \int I(V)dV$$

where m is the mass of the active material (i.e., Zr_xS_y), $V_a - V_b$ is the potential range, υ is the scan rate and $\int I(V)dV$ is the area within the curve.

3. Results and Discussions

3.1. The Morphology of the Zr_xS_y/CC

The scanning electron microscope (SEM) primarily uses a finely focused electron beam to scan the surface of a sample. It can observe the morphology and structure of the sample surface while also performing size observations. The SEM images illustrate the surface morphology and nanostructure of CC and Zr_xS_y/CC. Figure 2a shows that the CC surface contains several grooves, which serve as sites for deposition. Figure 2b presents the morphologies of Zr_xS_y nanoparticles directly synthesized on the fibers of the CC electrode. It demonstrates that the Zr_xS_y nanoparticles grow densely and uniformly on the fibers of the CC electrode. Figure 2c shows the distribution of particle size. It suggests that the Zr_xS_y nanoparticles have an average particle size of approximately 13.02 nm. The particle sizes mostly lie in the range from 3 nm to 23 nm.

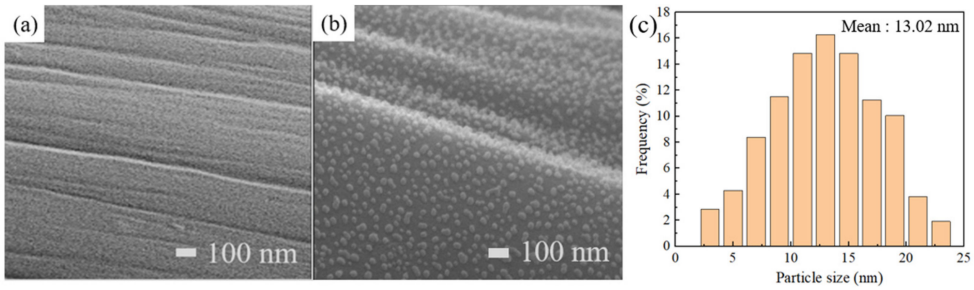

Figure 2. SEM images of (**a**) pristine CC and (**b**) Zr_xS_y/CC. (**c**) Particle size distribution of (**b**).

TEM is a technique that utilizes a high-energy electron beam to image ultra-thin samples. Its imaging resolution can reach atomic levels, up to 0.1 nanometers, making it an ideal instrument for observing the nanostructure of materials or analyzing lattice defects. Figure 3a presents the TEM images of Zr_xS_y nanoparticles. The homogeneous elemental distribution of Zr and S in the Zr_xS_y nanoparticles is observed by using elemental mapping profiles, as shown in Figure 3b,c. It shows that the Zr and S elements are uniformly distributed in the sample prepared for TEM analysis. HR-TEM can achieve atomic-level resolution, allowing for the observation of crystal structures, defects, and interfaces. To further investigate the crystal structure of the Zr_xS_y nanoparticles, HR-TEM images and selected area electron diffraction (SAED) patterns are provided in Figure 3d,e, respectively. Figure 3d demonstrates that the lattice spacings between two adjacent layers are approximately 0.235 nm, 0.259 nm, 0.298 nm, and 0.443 nm, which correspond to the (201), (200), (110), and (002) planes of ZrS_3, respectively. On the other hand, the interlayer spacings of 0.235 nm, 0.246 nm, and 0.259 nm correspond to the (008), (400), and (314) lattice planes of Zr_9S_2, respectively. The corresponding SAED pattern (Figure 3e) identifies and assigns the interplanar spacings corresponding to the diffraction rings.

XRD analysis is a technique that utilizes the interaction between X-rays and matter to study the structure of materials. It is primarily used to analyze crystal structures, phase compositions, and the nanostructure of materials. Figure 4 displayed the XRD patterns of the Zr_xS_y sample. The peaks of 20.5°, 30.3°, 34.6°, and 37.5° could be assigned to ZrS_3 (Monoclinic, PDF card No. 04-2864), and the corresponding crystal planes were (201), (200), (110), and (002), respectively. The other peaks of 30.6°, 35.4°, and 37.5° could be assigned to Zr_9S_2 (Tetragonal, PDF card No. 07-1763), and the corresponding crystal planes were (008), (400), and (314), respectively. The XRD patterns showed that the prepared Zr_xS_y sample

mainly comprised ZrS_3 and Zr_9S_2 phases. These results further confirm the HR-TEM analysis, indicating that the Zr_xS_y nanoparticles are composed of ZrS_3 and Zr_9S_2 phases.

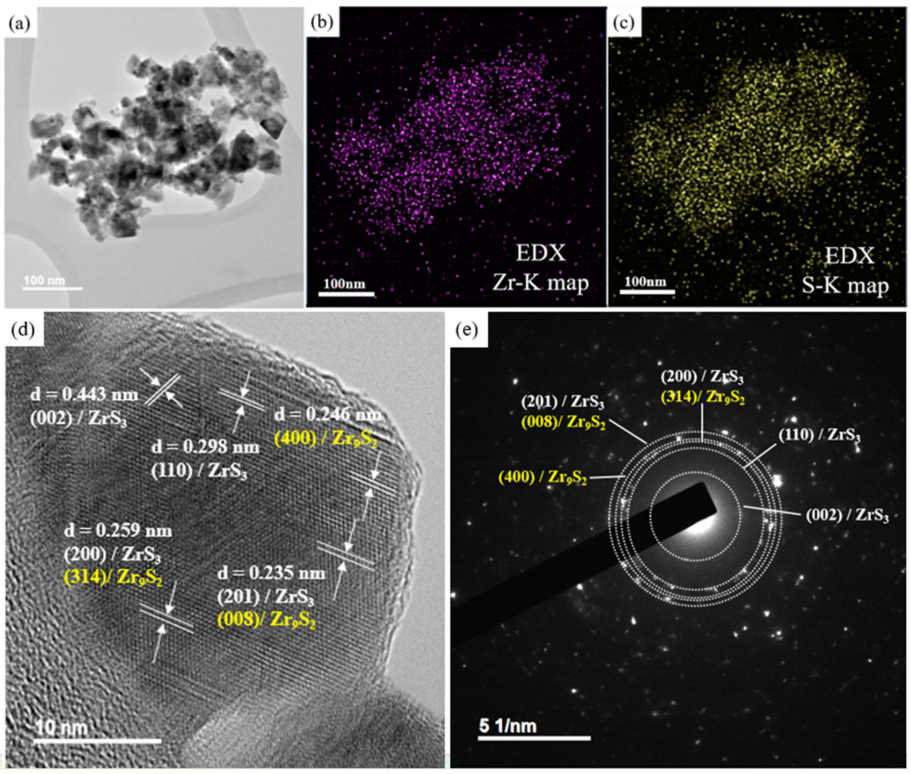

Figure 3. (**a**) TEM image of Zr_xS_y nanoparticles. (**b**) and (**c**) are the corresponding EDS mapping images of (**a**). (**d**) and (**e**) are HR-TEM images and the SAED patterns of Zr_xS_y nanoparticles, respectively.

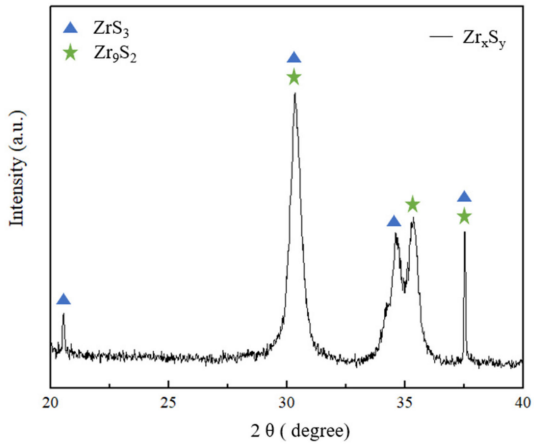

Figure 4. XRD pattern of Zr_xS_y.

3.2. Electrochemical Performance of Zr_xS_y/CC Electrode

To investigate the performance of the Zr_xS_y/CC electrode, we first characterized its electrochemical properties in a three-electrode system using 0.5 M H_2SO_4 aqueous solution as the electrolyte, Pt foil as the counter electrode, and a Ag/AgCl electrode as the reference electrode. Cyclic voltammetry is a highly sensitive electrochemical testing method with a wide range of applications. In qualitative analysis, it is commonly used to study redox processes, electron transfer dynamics, and other related phenomena. Figure 5a shows the variation in mass capacitance at different scan rates for the Zr_xS_y/CC electrode, where the CC and Zr_xS_y act as the conducting substrate and active material, respectively. All capacitance values were extracted from the CV curves, as shown in the inset of Figure 5b.

As the scan rate increased, the current density also increased; however, all CV curves maintained a similar shape, even at high scan rates, indicating that the Zr_xS_y continues to contribute to the capacitance. The calculated mass capacitance values were 406, 211, 88, 65, 57, and 46 C g^{-1} at scan rates of 5, 10, 50, 100, 150, and 200 mV s^{-1}, respectively. On the other hand, the specific surface area values of Zr_xS_y/CC and pristine CC are 47.58 m^2 g^{-1} and 39.01 m^2 g^{-1}, respectively. Thus, the area specific capacitance based on the specific surface area of Zr_xS_y can be estimated to be 47.37, 24.62, 10.27, 7.58, 6.65, and 5.37 C m^{-2} at scan rates of 5, 10, 50, 100, 150, and 200 mV s^{-1}, respectively.

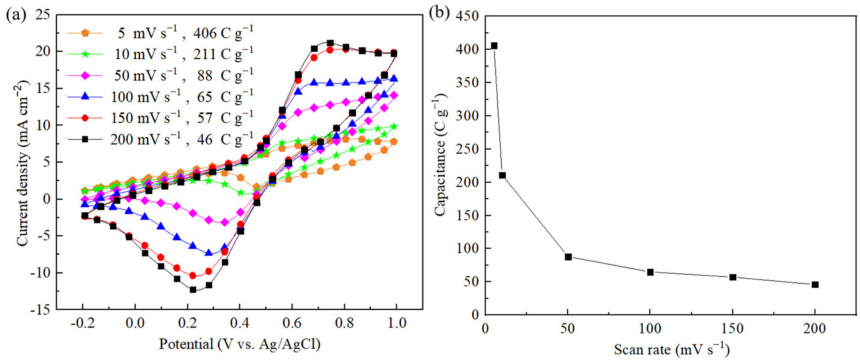

Figure 5. (**a**) CV analysis at various scan rates. (**b**) Variation of capacitance for various scan rates using the Zr_xS_y/CC, which is extracted from the CV curves.

In galvanostatic charge–discharge (GCD) experiments, the electrode is subjected to a constant current during both charging and discharging processes, while the voltage across the electrode is continuously monitored within a defined voltage range and over a set duration. Figure 6a shows the GCD curves of the Zr_xS_y/CC electrode; the capacitance values measured at a current density of 0.5 A g^{-1} and 1 A g^{-1} (within 1.0 V~−0.2 V) are 151 C g^{-1} and 134 C g^{-1}, respectively. The long-term stability of the Zr_xS_y/CC electrode was evaluated by cycling its charge–discharge behavior in a 0.5 M H_2SO_4 solution at a current density of 5 A g^{-1}, as shown in Figure 6b. After 1200 GCD cycles, the Zr_xS_y/CC electrode's capacitance retention is 63.88%.

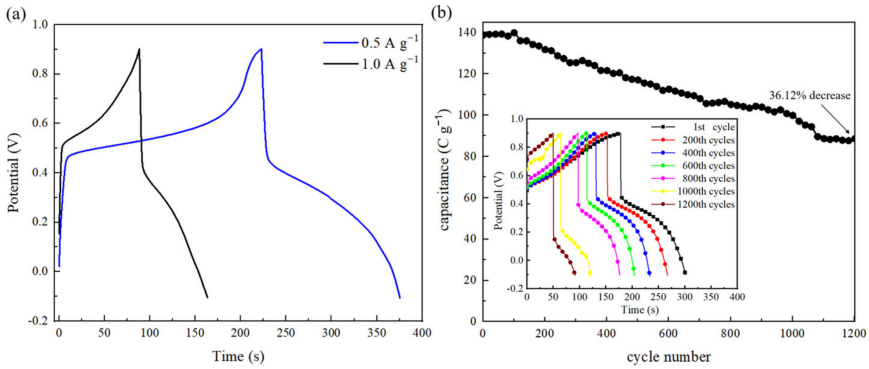

Figure 6. (**a**) GCD curves of the Zr_xS_y/CC electrode at current density of 0.5 A g^{-1} and 1 A g^{-1}. (**b**) GCD curves of the Zr_xS_y/CC electrode at high current density of 5 A g^{-1} for 1200 cycles.

4. Conclusions

Zirconium sulfide nanoparticles (Zr_xS_y) composed of ZrS_3 and Zr_9S_2 phases are prepared on the CC substrate via a one-step synthesis approach using the low-pressure chemical vapor deposition (LPCVD) technique. The SEM image reveals that the particle sizes are in the range of ca. 3~23 nm with an average value of ~13.02 nm. HR-TEM images and XRD patterns reveal Zr_xS_y nanoparticles possess the (201), (200), (110), and (002)

planes of ZrS_3 and the (008), (400), and (314) planes of Zr_9S_2. By using the Zr_xS_y/CC as a supercapacitor flexible electrode, the capacitance value obtained from CV measurement shows 406 C g^{-1} at a scan rate of 5 mV s^{-1}; the capacitance values obtained from GCD curves at a current density of 0.5 A g^{-1} and 1 A g^{-1} are 151 and 134 C g^{-1}, respectively. After 1200 GCD cycles (at 5 A g^{-1}), the Zr_xS_y/CC electrode's capacitance retention is 63.88%. To the best of our knowledge, this is the best performance of a Zr_xS_y-based supercapacitor electrode to date. These results highlight the promising potential of Zr_xS_y as a supercapacitor material for energy-storage technology.

Supplementary Materials: The following supporting information can be downloaded at: https://www.mdpi.com/article/10.3390/batteries11040138/s1, Figure S1. The demonstration photos of the flexibility of a device consisting of two Zr_xS_y/CC electrodes. Figure S2. Various light-emitting diodes (i.e., green, yellow, orange, and red lights) powered by a supercapacitor system consisting of ten Zr_xS_y/CC electrodes. Video files are also available in Supporting Information. Figure S3. XPS spectra of the synthesized Zr_xS_y. The curves are deconvoluted by Gaussian fitting. Figure S4. CV analysis of the pristine CC substrate at different scan rates. Figure S5. XRD patterns of Zr_xS_y/CC, the pristine CC, Zr_xS_y/sapphire carrier wafer, and sapphire carrier wafer. Table S1. A partial literature comparison list of supercapacitors using the related electrode materials, i.e., transition metal sulfides [52–64].

Author Contributions: Conceptualization, D.-S.T. and C.-P.L.; Methodology, D.-S.T. and C.-P.L.; Software, Y.-X.W., C.-J.H. and Z.-Y.C.; Validation, Y.-X.W., C.-J.H. and Z.-Y.C.; Formal analysis, Y.-X.W., C.-J.H. and Z.-Y.C.; Investigation, Y.-X.W., C.-J.H. and Z.-Y.C.; Resources, D.-S.T. and C.-P.L.; Data curation, Y.-X.W.; Writing—original draft, Y.-X.W.; Writing—review & editing, D.-S.T. and C.-P.L.; Visualization, D.-S.T. and C.-P.L.; Supervision, D.-S.T. and C.-P.L.; Project administration, D.-S.T. and C.-P.L.; Funding acquisition, D.-S.T. and C.-P.L. All authors have read and agreed to the published version of the manuscript.

Funding: This study is supported by the National Science and Technology Council (NSTC) of Taiwan, under the grant numbers 113-2221-E-845-001 and 113-2112-M-033-008.

Data Availability Statement: The original contributions presented in the study are included in the article and Supplementary Materials, further inquiries can be directed to the corresponding author.

Conflicts of Interest: The authors declare no conflicts of interest.

References

1. Shi, Y.; Sun, L.; Zhang, Y.; Si, H.; Sun, C.; Gu, J.; Gong, Y.; Li, X.; Zhang, Y. SnS_2 nanodots decorated on RGO sheets with enhanced pseudocapacitive performance for asymmetric supercapacitors. *J. Alloys Compd.* **2021**, *853*, 156903. [CrossRef]
2. Xu, Y.; Zhou, Y.; Guo, J.; Zhang, S.; Lu, Y. Preparation of SnS_2/g-C_3N_4 composite as the electrode material for Supercapacitor. *J. Alloys Compd.* **2019**, *806*, 343–349. [CrossRef]
3. Conway, B.E.; Birss, V.; Wojtowicz, J. The role and utilization of pseudocapacitance for energy storage by supercapacitors. *J. Power Sources* **1997**, *66*, 1–14. [CrossRef]
4. Mishra, R.K.; Baek, G.W.; Kim, K.; Kwon, H.-I.; Jin, S.H. One-step solvothermal synthesis of carnation flower-like SnS_2 as superior electrodes for supercapacitor applications. *Appl. Surf. Sci.* **2017**, *425*, 923–931. [CrossRef]
5. Gao, Q.; Ding, B.; Ertugrul, N.; Li, Y. Impacts of mechanical energy storage on power generation in wave energy converters for future integration with offshore wind turbine. *Ocean Eng.* **2022**, *261*, 112136. [CrossRef]
6. Majidi, M.; Rodriguez-Garcia, L.; Mosier, T.M.; Parvania, M. Coordinated operation of pumped-storage hydropower with power and water distribution systems. *Int. J. Electr. Power Energy Syst.* **2022**, *142*, 108297. [CrossRef]
7. Liu, L.; Zuo, S.; Wang, S. Engineering a highly conductive honeycomb network on carbon cloth-supported bimetallic sulfide nanorod arrays for flexible solid-state asymmetric supercapacitors with superior performance. *Chem. Eng. J.* **2024**, *502*, 158052. [CrossRef]
8. Jiang, Y.; Liu, J. Definitions of pseudocapacitive materials: A brief review. *Energy Environ. Mater.* **2019**, *2*, 30–37. [CrossRef]
9. Iro, Z.S.; Subramani, C.; Dash, S. A brief review on electrode materials for supercapacitor. *Int. J. Electrochem. Sci.* **2016**, *11*, 10628–10643. [CrossRef]

10. Halder, A.; Aman, M.; Jha, S.K. Enhancing supercapacitor performance with binder-free cobalt sulfide pseudo-capacitive electrodes: A path to sustainable energy storage. *J. Electroanal. Chem.* **2024**, *972*, 118631. [CrossRef]
11. Alam, S.; Khan, M.I.; Fiaz, F.; Iqbal, M.Z.; Alam, F.; Ahmad, Z.; Hegazy, H.H. Advancements in asymmetric supercapacitors: Material selection, mechanisms, and breakthroughs with metallic oxides, sulfides, and phosphates. *J. Energy Storage* **2023**, *72*, 108208.
12. Chen, Q.; Cai, D.; Zhan, H. Construction of reduced graphene oxide nanofibers and cobalt sulfide nanocomposite for pseudocapacitors with enhanced performance. *J. Alloys Compd.* **2017**, *706*, 126–132.
13. Tang, P.; Tan, W.; Deng, G.; Zhang, Y.; Xu, S.; Wang, Q.; Li, G.; Zhu, J.; Dou, Q.; Yan, X. Understanding pseudocapacitance mechanisms by synchrotron X-ray analytical techniques. *Energy Environ. Mater.* **2023**, *6*, e12619. [CrossRef]
14. González, A.; Goikolea, E.; Barrena, J.A.; Mysyk, R. Review on supercapacitors: Technologies and materials. *Renew. Sustain. Energy Rev.* **2016**, *58*, 1189–1206.
15. Shariq, M.; Alhashmialameer, D.; Adawi, H.; Alrahili, M.R.; Almashnowi, M.Y.; Alzahrani, A.; Sharma, M.; Ali, S.K.; Slimani, Y. Advancements in transition metal sulfide supercapacitors: A focused review on high-performance energy storage. *J. Ind. Eng. Chem.* **2024**, *144*, 269–291.
16. Bhojane, P. Recent advances and fundamentals of Pseudocapacitors: Materials, mechanism, and its understanding. *J. Energy Storage* **2022**, *45*, 103654.
17. Phor, L.; Kumar, A.; Chahal, S. Electrode materials for supercapacitors: A comprehensive review of advancements and performance. *J. Energy Storage* **2024**, *84*, 110698.
18. Raghavendra, K.; Alamara, K.; Al-Haik, M.Y.; Gopi, C.V.M.; Alzahmi, S.; Haik, Y.; Nutakki, T.U.K.; Obaidat, I.M.; Rao, K.M. Emphasis on the transition metal sulfides and their polymer composites as potential electrodes for supercapacitor applications. *J. Energy Storage* **2024**, *103*, 114312.
19. Lin, L.; Lei, W.; Zhang, S.; Liu, Y.; Wallace, G.G.; Chen, J. Two-dimensional transition metal dichalcogenides in supercapacitors and secondary batteries. *Energy Storage Mater.* **2019**, *19*, 408–423. [CrossRef]
20. Kour, P.; Kour, S.; Sharma, A.; Yadav, K. Electrochemical advancements in molybdenum disulfide via different transition metal (Cr, Mn, Fe, Co) doping for hybrid supercapacitors. *J. Alloys Compd.* **2024**, *981*, 173740.
21. Sajjad, M.; Amin, M.; Javed, M.S.; Imran, M.; Hu, W.; Mao, Z.; Lu, W. Recent trends in transition metal diselenides (XSe_2: X = Ni, Mn, Co) and their composites for high energy faradic supercapacitors. *J. Energy Storage* **2021**, *43*, 103176.
22. Sheikh, Z.A.; Katkar, P.K.; Kim, H.; Rehman, S.; Khan, K.; Chavan, V.D.; Jose, R.; Khan, M.F.; Kim, D.-K. Transition metal chalcogenides, MXene, and their hybrids: An emerging electrochemical capacitor electrodes. *J. Energy Storage* **2023**, *71*, 107997.
23. Kamila, S.; Kandasamy, M.; Chakraborty, B.; Jena, B.K. Recent development on engineered TMDs for charge storage performance: Experimental and theoretical investigations. *J. Energy Storage* **2024**, *89*, 111614.
24. Liu, L.; Li, H.; Jiang, S.; Zhao, Q.; Jiang, T. Design of high-performance transition metal sulfide electrode materials and its application in supercapacitors. *J. Power Sources* **2024**, *606*, 234560.
25. Ali, Z.; Iqbal, M.Z.; Hegazy, H. Recent advancements in redox-active transition metal sulfides as battery-grade electrode materials for hybrid supercapacitors. *J. Energy Storage* **2023**, *73*, 108857.
26. Zhang, C.; He, J.; Wang, G.; Hong, X.; Zhao, C. Recent advances in heteroatom doped transition metal sulfides for high-performance supercapacitors. *J. Energy Storage* **2024**, *104*, 114562.
27. Iqbal, M.Z.; Aziz, U.; Amjad, N.; Aftab, S.; Wabaidur, S.M. Porous activated carbon and highly redox active transition metal sulfide by employing multi-synthesis approaches for battery-supercapacitor applications. *Diam. Relat. Mater.* **2023**, *136*, 110019.
28. Gao, Y.; Zhao, L. Review on recent advances in nanostructured transition-metal-sulfide-based electrode materials for cathode materials of asymmetric supercapacitors. *Chem. Eng. J.* **2022**, *430*, 132745.
29. Shao, Q.; Liu, X.; Dong, J.; Liang, L.; Zhang, Q.; Li, P.; Yang, S.; Zang, X.; Cao, N. Vulcanization Conditions of Bimetallic Sulfides Under Different Sulfur Sources for Supercapacitors: A Review. *J. Electron. Mater.* **2023**, *52*, 1769–1784. [CrossRef]
30. He, Q.; Wu, X. Ni_3S_2@NiMo-LDH Composite for Flexible Hybrid Capacitors. *Batteries* **2024**, *10*, 230. [CrossRef]
31. Mohan, M.; Shetti, N.P.; Aminabhavi, T.M. Phase dependent performance of MoS_2 for supercapacitor applications. *J. Energy Storage* **2023**, *58*, 106321. [CrossRef]
32. Nabi, G.; Ali, W.; Tanveer, M.; Iqbal, T.; Rizwan, M.; Hussain, S. Robust synergistic effect of TiS_2/MoS_2 hierarchal micro-flowers composite realizing enhanced electrochemical performance. *J. Energy Storage* **2023**, *58*, 106316. [CrossRef]
33. Wang, H.; Tian, L.; Zhao, X.; Ali, M.; Feng, H.; Han, S.; Xing, Z.; Kumar, S.; Ding, J. Synthesis of MoS_2/CoS composite electrode and its application for supercapacitors. *J. Alloys Compd.* **2023**, *960*, 170835.
34. Liu, X.; Ma, X.; Liu, G.; Zhang, X.; Tang, X.; Li, C.; Zang, X.; Cao, N.; Shao, Q. Polyaniline spaced MoS_2 nanosheets with increased interlayer distances for constructing high-rate dual-ion batteries. *J. Mater. Sci. Technol.* **2024**, *182*, 220–230. [CrossRef]
35. Duangchuen, T.; Karaphun, A.; Wannasen, L.; Kotutha, I.; Swatsitang, E. Effect of SnS_2 concentrations on electrochemical properties of SnS2/RGO nanocomposites synthesized by a one-pot hydrothermal method. *Appl. Surf. Sci.* **2019**, *487*, 634–646.

36. Venkateshalu, S.; Kumar, P.G.; Kollu, P.; Jeong, S.K.; Grace, A.N. Solvothermal synthesis and electrochemical properties of phase pure pyrite FeS_2 for supercapacitor applications. *Electrochim. Acta* **2018**, *290*, 378–389. [CrossRef]
37. Wang, Y.; Zhang, M.; Ma, T.; Pan, D.; Li, Y.; Xie, J.; Shao, S. A high-performance flexible supercapacitor electrode material based on nano-flowers-like FeS_2/NSG hybrid nanocomposites. *Mater. Lett.* **2018**, *218*, 10–13.
38. Durga, I.K.; Rao, S.S.; Kalla, R.M.N.; Ahn, J.-W.; Kim, H.-J. Facile synthesis of FeS_2/PVP composite as high-performance electrodes for supercapacitors. *J. Energy Storage* **2020**, *28*, 101216. [CrossRef]
39. Niknam, E.; Naffakh-Moosavy, H.; Moosavifard, S.E.; Afshar, M.G. Amorphous V-doped Co_3S_4 yolk-shell hollow spheres derived from metal-organic framework for high-performance asymmetric supercapacitors. *J. Alloys Compd.* **2022**, *895*, 162720.
40. Mahieddine, A.; Adnane-Amara, L.; Tebaa, T.; Saba, C. Core-shell structured hierarchical Ni nanowires and NiS/Co3S4 microflowers arrays as a high-performance supercapacitor electrode. *J. Energy Storage* **2023**, *57*, 106173. [CrossRef]
41. Wu, W.; Liu, T.; Diwu, J.; Li, C.; Zhu, J. Metal-organic framework–derived $NiCo_2S_4$@Co_3S_4 yolk-shell nanocages/$Ti_3C_2T_x$ MXene for high-performance asymmetric supercapacitors. *J. Alloys Compd.* **2023**, *954*, 170213. [CrossRef]
42. Wang, H.; Liang, M.; Duan, D.; Shi, W.; Song, Y.; Sun, Z. Rose-like Ni_3S_4 as battery-type electrode for hybrid supercapacitor with excellent charge storage performance. *Chem. Eng. J.* **2018**, *350*, 523–533. [CrossRef]
43. Das, A.; Maitra, A.; Mondal, A.; De, A.; Maity, P.; Khatua, B.B. Hydrothermal synthesis of Cu_2S/NiS/Ni_3S_4 as high performance supercapacitor application. *J. Energy Storage* **2024**, *92*, 112293. [CrossRef]
44. Liu, C.; Zhang, X.; Cheng, Y.; Hao, X.; Yang, P. NiS/Ni_3S_4 decorated double-layered hollow carbon spheres for efficient electrochemical hydrogen evolution reaction and supercapacitor. *Electrochim. Acta* **2024**, *477*, 143751. [CrossRef]
45. Yu, X.Y.; Lou, X.W. Mixed metal sulfides for electrochemical energy storage and conversion. *Adv. Energy Mater.* **2018**, *8*, 1701592. [CrossRef]
46. Rui, X.; Tan, H.; Yan, Q. Nanostructured metal sulfides for energy storage. *Nanoscale* **2014**, *6*, 9889–9924. [CrossRef]
47. Barik, R.; Ingole, P.P. Challenges and prospects of metal sulfide materials for supercapacitors. *Curr. Opin. Electrochem.* **2020**, *21*, 327–334. [CrossRef]
48. Li, X.; Elshahawy, A.M.; Guan, C.; Wang, J. Metal phosphides and phosphates-based electrodes for electrochemical supercapacitors. *Small* **2017**, *13*, 1701530. [CrossRef]
49. Jin, W.; Maduraiveeran, G. Recent advances of porous transition metal-based nanomaterials for electrochemical energy conversion and storage applications. *Mater. Today Energy* **2019**, *13*, 64–84. [CrossRef]
50. Habib, M.; Ullah, S.; Khan, F.; Rafiq, M.I.; Balobaid, A.S.; Alshahrani, T.; Muhammad, Z. Supercapacitor electrodes based on single crystal layered ZrX_2 (X = S, Se) using chemical vapor transport method. *Mater. Sci. Eng. B* **2023**, *298*, 116904. [CrossRef]
51. Mariappan, V.K.; Krishnamoorthy, K.; Pazhamalai, P.; Sahoo, S.; Kesavan, D.; Kim, S.-J. Two dimensional famatinite sheets decorated on reduced graphene oxide: A novel electrode for high performance supercapacitors. *J. Power Sources* **2019**, *433*, 126648.
52. Xing, J.-C.; Zhu, Y.-L.; Zhou, Q.-W.; Zheng, X.-D.; Jiao, Q.-J. Fabrication and shape evolution of CoS_2 octahedrons for application in supercapacitors. *Electrochim. Acta* **2014**, *136*, 550–556.
53. Zeng, X.; Yang, B.; Li, X.; Yu, R. Three-dimensional hollow CoS_2 nanoframes fabricated by anion replacement and their enhanced pseudocapacitive performances. *Electrochim. Acta* **2017**, *240*, 341–349.
54. Pujari, R.B.; Lokhande, V.C.; Patil, U.M.; Lee, D.W.; Lokhande, C.D. Controlled sulfurization of $MnCO_3$ microcubes architectured MnS2 nanoparticles with 1.7 fold capacitance increment for high energy density supercapacitor. *Electrochim. Acta* **2019**, *301*, 366–376.
55. Javed, M.S.; Han, X.; Hu, C.; Zhou, M.; Huang, Z.; Tang, X.; Gu, X. Tracking Pseudocapacitive Contribution to Superior Energy Storage of MnS Nanoparticles Grown on Carbon Textile. *ACS Appl. Mater. Interfaces* **2016**, *8*, 24621–24628.
56. Mohan, V.V.; Rakhi, R.B. WS_2/Conducting polymer nanocomposite-based flexible and binder-free electrodes for high-performance supercapacitors. *Electrochim. Acta* **2024**, *498*, 144657. [CrossRef]
57. Mohan, V.; Mohan, M.; Anjana, P.; Rakhi, R. WS_2 nanoflowers as efficient electrode materials for supercapacitors. *Energy Technol.* **2021**, *10*, 2100976. [CrossRef]
58. Upadhyay, K.K.; Nguyen, T.; Silva, T.M.; Carmezim, M.J.; Montemor, M.F. Pseudocapacitive response of hydrothermally grown MoS_2 crumpled nanosheet on carbon fiber. *Mater. Chem. Phys.* **2018**, *216*, 413–420.
59. Krishnamoorthy, K.; Veerasubramani, G.K.; Radhakrishnan, S.; Kim, S.J. Supercapacitive properties of hydrothermally synthesized sphere like MoS_2 nanostructures. *Mater. Res. Bull.* **2014**, *50*, 499–502.
60. Hussain, I.; Mohapatra, D.; Dhakal, G.; Lamiel, C.; Sayed, M.S.; Sahoo, S.; Mohamed, S.G.; Kim, J.S.; Lee, Y.R.; Shim, J.-J. Uniform growth of ZnS nanoflakes for high-performance supercapacitor applications. *J. Energy Storage* **2021**, *36*, 102408.
61. Chauhan, H.; Singh, M.K.; Kumar, P.; Hashmi, S.A.; Deka, S. Development of SnS_2/RGO nanosheet composite for cost-effective aqueous hybrid supercapacitors. *Nanotechnology* **2017**, *28*, 025401. [PubMed]
62. Lonkar, S.P.; Pillai, V.V.; Patole, S.P.; Alhassan, S.M. Scalable In Situ Synthesis of 2 D Type Graphene Wrapped SnS_2 Nanohybrids for Enhanced Supercapacitor and Electrocatalytic Applications. *ACS Appl. Energy Mater.* **2020**, *3*, 4995–5005.

63. Peng, L.; Ji, X.; Wan, H.; Ruan, Y.; Xu, K.; Chen, C.; Miao, L.; Jiang, J. Nickel sulfide nanoparticles synthesized by microwave-assisted method as promising supercapacitor electrodes: An experimental and computational study. *Electrochim. Acta* **2015**, *182*, 361–367.
64. Seemab, M.; Nabi, G. Structural transformations and enhanced electrochemical performance of Co doped NiS_2 nanosheets for supercapacitor applications. *Ceram. Int.* **2024**, *50*, 27856–27866.